Advanced Materials Technologies

ADVANCED MATERIALS TECHNOLOGIES
www.advmattechnol.com

RESEARCH ARTICLE OPEN ACCESS

Cellulose-Nanofiber-Based Layered Sub-Terahertz Absorbing Sheets for B5G/6G Applications

Kosaku Kato[1] | Shiyu Feng[1] | Zixi Zhao[1] | Verdad C. Agulto[1] | Ami Mizui[2] | Takaaki Kasuga[2] | Shun Ishioka[2] | Masaya Nogi[2] | Ichiro Ota[1,3] | Motoharu Haga[4] | Minoru Ueshima[3] | Makoto Nakajima[1]

[1]Institute of Laser Engineering, The University of Osaka, Suita, Osaka, Japan | [2]SANKEN (The Institute of Scientific and Industrial Research), The University of Osaka, Ibaraki, Osaka, Japan | [3]Daicel Corporation, Minato-ku, Tokyo, Japan | [4]Daicel Corporation, Kita-ku, Osaka, Japan

Correspondence: Makoto Nakajima (nakajima.makoto.ile@osaka-u.ac.jp)

Received: 29 August 2025 | **Revised:** 29 October 2025 | **Accepted:** 14 November 2025

Keywords: carbon-nanotubes | cellulose-nanofibers | terahertz absorbers

ABSTRACT

For the sustainable development of beyond fifth-generation (B5G) or sixth-generation (6G) wireless communication technologies operating in the sub-terahertz and terahertz range, it is highly desirable to utilize environmentally friendly materials in B5G/6G devices. Here, we report a sub-terahertz absorbing sheet made of biodegradable cellulose-nanofiber (CNF), which can be useful for achieving electromagnetic compatibility (EMC) in B5G/6G devices in a green manner. The absorber consists of one pure CNF layer sandwiched between two layers of carbon-nanotube (CNT)-dispersed CNF layers. The CNT concentration is engineered to be low (0.15 wt.%) in the layer on the wave-incident side and high (6 wt.%) in the layer on the opposite side, emulating the resistive and reflective layers of a Salisbury screen absorber, respectively. The total thickness of our absorber is as thin as 120 μm. Terahertz time-domain spectroscopy (THz-TDS) reveals its good shielding effectiveness of 28.5 dB, low reflectance of 2.5%, and high absorptance of 97.4% at 300 GHz. Additionally, an absorptance higher than 80% is achieved over a broadband frequency range from 250 to 480 GHz. Good agreement between the measured results and calculated results based on the ABCD matrix method confirms that the cancellation of reflected waves is realized as designed.

1 | Introduction

The amount of wireless data traffic has increased dramatically in recent years, and this trend is expected to continue growing exponentially in the future [1, 2]. To increase the capacity and speed of wireless communication, broader frequency bands are required beyond the currently used range, which extends up to tens of gigahertz. Therefore, in the next generation wireless communication called beyond fifth generation (B5G) or sixth generation (6G), the frequency range is planned to extend into the sub-terahertz and terahertz regions [3–5]. In the development of B5G/6G devices, electromagnetic compatibility (EMC) for terahertz waves must be ensured: the waves emitted from a B5G/6G transmitter should not cause malfunction in other devices, and the communication should not be disrupted by external electromagnetic noise reaching a B5G/6G receiver. For EMC in B5G/6G devices, it is essential to appropriately block unwanted terahertz waves. Although a conductive film such as metal can shield terahertz waves, its high reflectance may cause reflected waves to adversely affect the emitter itself or other nearby devices. To avoid this problem, terahertz wave absorbers with both good shielding effectiveness (SE) and low reflectance are required.

In the sub-terahertz range used for B5G/6G communication, absorbers based on magnetic responses using conventional magnetic materials are not applicable, highlighting the importance of utilizing artificially structured materials. Various structures

have been reported as terahertz wave absorbers, including those consisting of metallic 2D [6–9] or 3D [10, 11] micropatterned metamaterials, dielectric resonator arrays with spherical [12–14] and pillar-shaped [15–17] geometries, magnetic materials tailored for terahertz absorption [18, 19], carbon foams [20] and polymer composites [21, 22]. Among these, a three-layer sheet called the Salisbury screen absorber (SSA) [23] is notable for its simple structure. An SSA consists of a front resistive layer, a middle dielectric spacer layer, and a backside reflective layer. The front layer is separated from the backside layer by a quarter-wavelength of the absorbing frequency ($\lambda/4$) so that the waves reflected from these layers cancel each other out. SSAs can achieve high absorptance without the need to synthesize materials or micropattern metamaterials that resonate at the target frequency. Due to its structural simplicity and scalability, the SSA configuration is particularly attractive for integration into compact B5G/6G devices. There have been reports on SSAs for terahertz waves, including those that use a thin metal film [24], graphene [25], or an organic crystal [26] as the front resistive layer.

From an environmental perspective, previously existing sub-terahertz and terahertz absorbers have issues of concern. Most of them are composed of a combination of metals and insulators, which poses a problem in the disposal process: since metal is non-burnable and separating the metal and insulator components is difficult, these absorbers need to be landfilled in a whole for disposal. This runs counter to worldwide efforts on waste reduction and has a risk of generating microplastic particles when the insulator part is made of plastic. Though there are reports on all-dielectric terahertz absorbers [16, 17], they are made of non-degradable semiconductors and plastics, and the above-mentioned disposal problem still remains. To solve B5G/6G EMC problems in a sustainable manner, we have set the objective of our research as the development of an absorber made from materials with a lower environmental impact than previous approaches.

In this work, we developed a sub-terahertz absorbing sheet consisting of cellulose nanofiber (CNF). CNF has received a lot of attention in recent years because of its biodegradability, as well as its lightweight, high mechanical strength, and heat resistance. CNF is a nanoscale fiber of crystalline cellulose with a typical width of 3–15 nm and can be extracted from natural wood [27, 28]. Various applications of CNF have been reported including electronic devices such as displays [29] and sensors [30, 31], reinforcement of plastics [32, 33], moldings [34], and electrode coating for circuit protection [35]. Herein, we designed and fabricated an SSA-type absorber using thin films of carbon-nanotube (CNT)-dispersed CNF (CNT:CNF) as resistive and reflective layers, and pure CNF as a spacer layer. Owing to the excellent film-forming ability of CNF, its dielectric function and loss tangent can be widely tuned by incorporating a small amount of CNT, enabling the design of absorbers with tailored electromagnetic properties. Our absorber is targeted at the frequency range around 300 GHz (0.3 THz), for which the IEEE 802.15.3d standard was released as part of the standardization effort for 6G communication [36, 37]. Though CNF-based electromagnetic wave absorbers have been reported so far [38–41], most of them are designed for microwaves with a frequency range of several to several tens of gigahertz, and their thickness exceeded 1 mm. While recent studies have reported terahertz CNF-based absorbers incorporating structures such as metal-organic frameworks with MXene [42] or graphene-based metamaterials [43], our absorber adopts a simpler three-layer structure composed solely of CNF and CNT, offering advantages in fabrication. Our sub-terahertz absorber has a small thickness of 120 μm, suitable for use in compact devices, and still shows a good SE of 28.5 dB, low reflectance of 2.5%, and a high absorptance of 97.4% at 300 GHz. The novelty of our absorber lies in its combination of structural simplicity, biodegradability, and thin-film scalability, demonstrating the potential for practical, compact, and sustainable B5G/6G devices.

2 | Results and Discussion

2.1 | Dielectric Functions of Single-Layer CNT:CNF Films

As a preliminary step toward designing a three-layer absorber, we first evaluated the dielectric functions of single-layer pure CNF and CNT:CNF films using terahertz time-domain spectroscopy (THz-TDS) [44, 45], the details of which are described in the Experimental Section. The measured dielectric functions of the CNF films with 0, 0.15, and 6 wt.% CNT are shown in Figure 1a. The dielectric function of the CNF film without CNT was almost independent of frequency, and the real part (ε') and loss tangent ($\tan\delta$) are 4.4 and 0.05 at 300 GHz, respectively. When only 0.15 wt.% CNT was mixed into CNF, the values of ε' and $\tan\delta$ were remarkably increased to 10.0 and 0.63 at 300 GHz, respectively. In addition, the incorporation of CNT resulted in a monotonically decreasing spectrum of ε' with increasing frequency. This frequency dependence, also observed in previous reports for a CNT-dispersed polymer [46, 47], reflects the damped-oscillator-like behavior of the CNT's dielectric function. When 6 wt.% CNT was mixed into CNF, the ε' and $\tan\delta$ were further increased, reaching 270 and 1.6 at 300 GHz, respectively. The values of ε' and $\tan\delta$ at 300 GHz are summarized in Figure 1b. These results reveal that the terahertz dielectric properties of CNF films can be tuned in a wide dynamic range by adding a small amount of CNT.

2.2 | Design and Fabrication of the Three-Layer Absorber

We designed an absorber schematically illustrated in Figure 2a. A pure CNF layer is sandwiched between layers having a low-concentration (LC)-CNT:CNF and high-concentration (HC)-CNT:CNF. The sub-terahertz electromagnetic wave is to be incident from the LC-CNT:CNF layer side. The LC-CNT:CNF, pure CNF and HC-CNT:CNF layers were adopted with the expectation that they would function as a resistive layer, spacer layer and reflective layer of an SSA absorber, respectively.

We investigated the specific design of the three-layer structure by calculating the SE and reflectance with the ABCD matrix method, which enables us to estimate the transmittance and reflectance of a layered structure taking all the reflections at interfaces into account [48, 49]. Since both the CNF and CNT are nonmagnetic, the relative permeabilities of all the layers are considered to be 1.

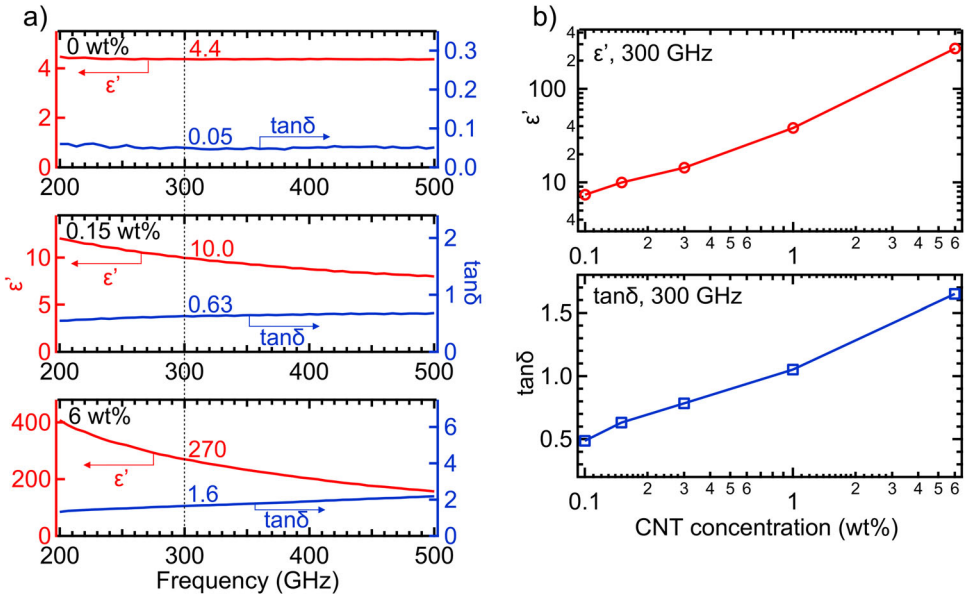

FIGURE 1 | (a) Dielectric functions of CNF films with 0 wt.% (top), 0.15 wt.% (middle) and 6 wt.% (bottom) CNT. The real part (ε') and loss tangent ($\tan\delta$) of the dielectric function are shown on the left and right axis, respectively. The vertical dotted line and the numbers next to it indicate 300 GHz and the values of ε' and $\tan\delta$ at 300 GHz, respectively. (b) ε' (top) and $\tan\delta$ (bottom) of the CNT:CNF films at 300 GHz as a function of CNT concentration from 0.1 to 6 wt.%.

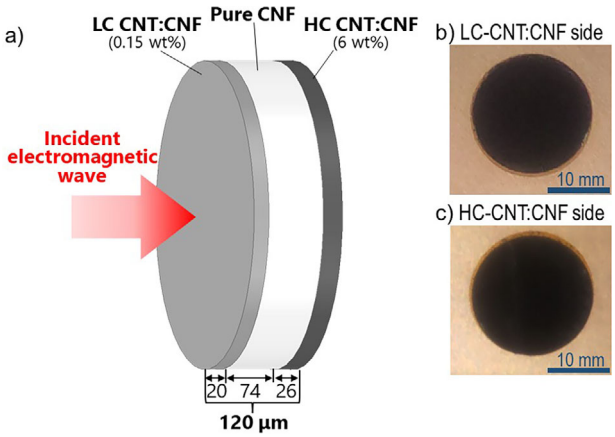

FIGURE 2 | (a) Schematic of the absorber structure. LC- and HC-CNT:CNF refer to CNF layers containing low and high concentrations of CNT, respectively. (b,c) Photographs of the fabricated absorber taken from the LC-CNT:CNF side and the HC-CNT:CNF side, respectively.

Then the ABCD matrix of the lth layer ($l = 1, 2, 3$) with complex dielectric constant ε_l and thickness d_l is given by

$$\begin{pmatrix} A_l & B_l \\ C_l & D_l \end{pmatrix} = \begin{pmatrix} \cosh\gamma_l d_l & z_l \sinh\gamma_l d_l \\ (1/z_l)\sinh\gamma_l d_l & \cosh\gamma_l d_l \end{pmatrix} \quad (1)$$

with normalized characteristic impedance $z_l = 1/\sqrt{\varepsilon_l}$ and propagation constant $\gamma_l = -i \cdot 2\pi f\sqrt{\varepsilon_l}/c$. Here, i is the imaginary unit, f is the frequency of the electromagnetic wave, and c is the speed of light. Then the ABCD matrix of the three-layer structure becomes

$$\begin{pmatrix} A & B \\ C & D \end{pmatrix} = \begin{pmatrix} A_1 & B_1 \\ C_1 & D_1 \end{pmatrix}\begin{pmatrix} A_2 & B_2 \\ C_2 & D_2 \end{pmatrix}\begin{pmatrix} A_3 & B_3 \\ C_3 & D_3 \end{pmatrix} \quad (2)$$

and the power transmittance T and reflectance R of this structure can be calculated as

$$T = \left|\frac{2}{A+B+C+D}\right|^2, R = \left|\frac{A+B-C-D}{A+B+C+D}\right|^2 \quad (3)$$

The SE is calculated from the power transmittance T as

$$SE = -10\log_{10}T \quad (4)$$

Based on these formulas, we explored combinations of CNT concentrations and layer thicknesses that would yield a high SE and low reflectance at 300 GHz. We also aimed to keep the total thickness of the absorber as small as ~0.1 mm for usability, while ensuring that the thickness of each layer remained above 10 μm, taking the feasibility of fabrication into account. The optimization was carried out with the help of the simulated annealing (SA) algorithm, implemented in a data analysis software (Wavemetrics, Igor Pro). SA is a probabilistic optimization method that helps explore the solution space to find near-optimal configurations. In our study, the thicknesses of the three layers d_1,d_2, and d_3 were treated as variable parameters. The algorithm was run repeatedly to identify combinations that simultaneously achieve high SE, low reflectance, and small total thickness. From the resulting candidates, we selected a promising configuration for optimal performance, while rejecting solutions with excessively thick or thin layers. As a result, it was found that a good SE of ~30 dB and a near-zero reflection can be achieved at 300 GHz with the combination of 20-μm-thick 0.15 wt.%-CNT:CNF layer, 74-μm-thick pure CNF layer, and a 26-μm-thick 6 wt.%-CNT:CNF layer. The total thickness of the 3 layers is 120 μm. Note that the optical path length of the pure CNF layer, calculated as 155 μm from its thickness and dielectric constant $\varepsilon' = 4.4$, is shorter than the quarter of the wavelength at 300 GHz, $\lambda/4 = 250$ μm. This is because in our design the LC-CNT:CNF layer has a

non-negligible thickness, and waves can partially penetrate into the HC-CNT:CNF layer as discussed later. Thus, these layers also contribute to the effective spacer thickness in the SSA structure, helping to satisfy the $\lambda/4$ condition.

The absorber sheet was fabricated by stacking the films of LC-CNT:CNF, pure CNF, and HC-CNT:CNF as described in the Experimental Section. The photographs of the absorber taken from the LC-CNT and HC-CNT sides are shown in Figure 2b,c, respectively. In appearance there is no clear difference between these two sides. Figure S1a,b present microscale images of the LC-CNT and HC-CNT side of the absorber acquired by a scanning electron microscopy (JEOL, JSM-7400FS), respectively. The surfaces appear flat, with no distinct microstructures observed. The thickness of the absorber measured with a thickness meter (Mitutoyo, 547-401. Resolution 1 μm) was ~120 μm, agreeing with the designed thickness. Cross-sectional SEM observation further confirmed that the layer thicknesses were in accordance with the design (Figure S1c). The thermal degradation behavior and mechanical properties of the absorber were evaluated as described in Experimental Section. As shown in Figures S2 and S3, the absorber exhibited thermal and mechanical stability comparable to those of previously reported CNF films [50, 51], indicating its applicability for practical use.

2.3 | Measurement and Simulation Results of the Absorber Performance

We evaluated the performance of the fabricated absorber sheet using THz-TDS (see Experimental Section). The solid red curves in Figure 3a show the spectra of SE, reflectance, and absorptance of the sample when the electromagnetic wave was incident from the LC-CNT:CNF layer side. The SE (top panel in Figure 3a) showed a tendency to increase with frequency, from 23.4 dB at 150 GHz to 41.5 dB at 500 GHz. At 300 GHz it reached 28.5 dB, which corresponds to a transmittance of only 0.14%. The reflectance spectrum (middle panel in Figure 3a) had a broad dip around 330 GHz owing to the cancellation of reflected waves in the three-layer structure. The reflectance at 300 GHz was suppressed down to 2.5%. As a result of the high SE and low reflectance, the absorptance at 300 GHz reached as high as 97.4% (bottom panel in Figure 3a). For comparison, we also show the spectra when the wave was incident from the HC-CNT side as dashed blue curves in Figure 3. Though the SE was virtually independent of the incidence side, the reflectance and absorptance became much higher and lower, respectively, than the case of LC-CNT:CNF layer side incidence. The reason for this large dependence on the incidence side is discussed later. Note that the observed performance of our absorber in the case of LC-CNT:CNF layer side incidence is fairly good at frequencies away from 300 GHz: SE higher than 25 dB and absorptance higher than 80% are achieved across the frequency range from 250 to 480 GHz. In addition, the peak absorptance of our absorber reaches 99.4% at 333 GHz, which is comparable to or even exceeds those of previously reported SSA-based terahertz absorbers using metal, with reported values of 99.4%, 97%, and 92.9% in References [24–26], respectively. This is also better than those of previously reported all-dielectric absorbers, 97.5% and 96% in References [16, 17], respectively.

To examine the measurement results, we compared them with the results of numerical calculations. Figure 3b shows the calculated SE, reflectance, and absorptance spectra calculated using the ABCD matrix method described above. They are overall in good agreement with the experimental results in Figure 3a, suggesting that the absorber is functioning as it is designed. To gain a deeper understanding of the working behavior of this absorber, we also calculated the depth profile of the energy loss for the incident 300-GHz electromagnetic wave with a power density of 1 W/m^2 using the finite element method (Figure 4). When the wave impinges on the absorber from the LC-CNT:CNF layer side (solid red curve), a large energy loss occurs in the LC-CNT:CNF layer. This indicates that this layer mainly dissipates the energy of the electromagnetic wave into heat, as the resistive layer in ordinary SSAs does. The energy loss in the pure CNF layer is small due to its small loss tangent, showing that this layer mainly works as the spacer layer of the SSAs. There is a non-negligible energy loss in the HC-CNT:CNF layer, indicating that a portion of the wave penetrates into this layer and loses its energy. In this sense, the HC-CNT:CNF layer in our absorber functions not only as a reflective layer but also partially serves as a spacer and resistive layer. On the other hand, when the wave is incident from the HC-CNT:CNF side (dashed blue curve), energy loss only occurs around the surface of the HC-CNT:CNF layer, and the total amount of the energy loss density is significantly smaller than in the case of LC-CNT:CNF layer side incidence. This is because the waves are mostly reflected by the HC-CNT:CNF layer, while little can reach the LC-CNT:CNF layer, and thus the cancellation of the waves reflected from these layers does not occur. This result emphasizes the importance of the first LC-CNT:CNF layer and the second pure CNF layer of our absorber in achieving high absorption.

3 | Conclusions

We developed a CNF-based three-layer-type sub-terahertz wave absorbing sheet. Excellent properties of 28.5-dB SE and 97.4% absorptance at 300 GHz were achieved by the 120 μm-thick film consisting of only CNF and a small amount of CNT. The environmental benefit of CNF is not only its biodegradability but also its producibility from natural wood, which makes it a sustainable material in contrast to petroleum-derived plastics. The light and thin properties of our absorber will also contribute to decreasing the weight and size of B5G/6G devices, thus reducing the energy consumption necessary for their transport. Our study demonstrated that CNF-based absorbers can provide an eco-friendly choice for EMC achievement in the sub-terahertz region and help pro-environmental development of B5G/6G communication technologies.

4 | Experimental Section

4.1 | Sample Fabrication

CNT:CNF films for each layer of the absorber were prepared as follows: 0.4 wt.% TEMPO (2,2,6,6-tetramethylpiperidine-1-oxyl radical)-oxidized CNF (DKS Co., Ltd., RHEOCRYSTA I-2SX) / water dispersion was used for film preparation. Single-walled CNT (Kusumoto Chemicals, Ltd., WPB-043) was added to the CNF/water dispersion at a ratio of 0.15 and 6 wt.% relative to

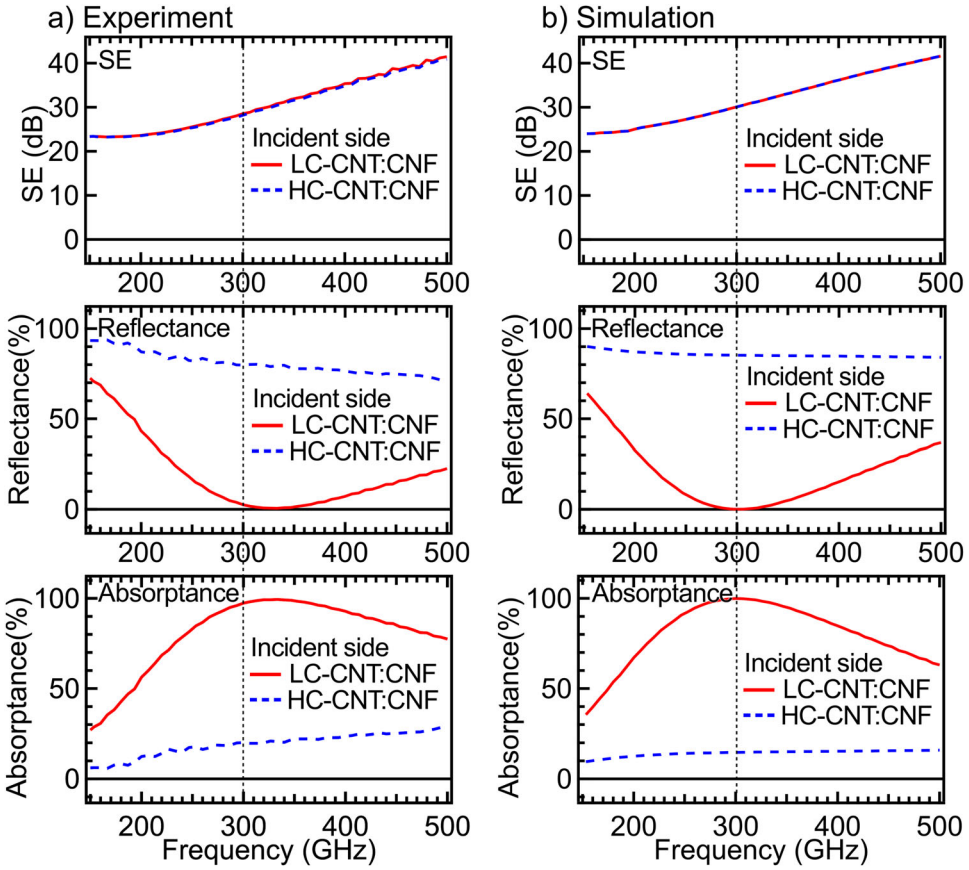

FIGURE 3 | (a) Measurement results of the SE (top), reflectance (middle), and absorptance (bottom) of the fabricated absorber. The solid red curves and dashed blue curves indicate the results when the electromagnetic wave impinges on the sample from the LC-CNT:CNF and HC-CNT:CNF layer sides, respectively. The vertical dotted line indicates 300 GHz. (b) Same as (a) but numerical simulation results.

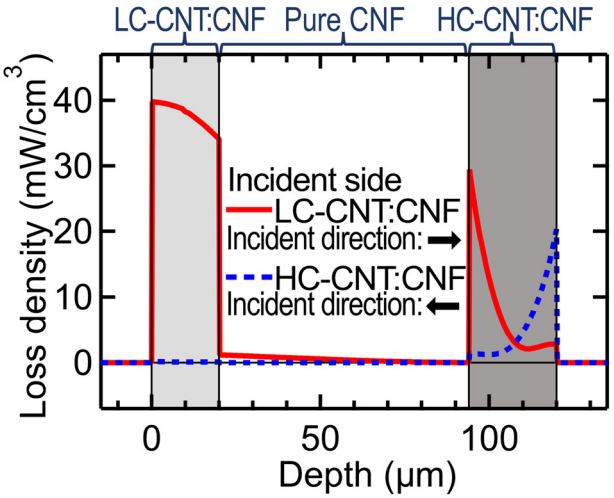

FIGURE 4 | Simulation results of the volume loss density distribution as a function of depth when the 300-GHz electromagnetic wave with a power density of 1 W/m^2 impinges on the sample from the LC-CNT:CNF layer side (solid red curve) and HC-CNT:CNF layer side (dashed blue curve).

CNF. The CNT/CNF/water dispersion was homogenized using an ultrasonic homogenizer (Nissei Corp., US-300E) at 100% output for 1 min. Then CNF/water dispersion and CNT/CNF/water dispersion were dried at a temperature of 10°C and relative humidity of 90% to form films. CNF and CNT:CNF films with the desired thickness were prepared by adjusting the amount of dispersion before drying. The lamination was performed using the same procedure as previously reported in Ref. [51]. Namely, to combine the films into a layered absorber, the films were stacked and soaked in a mixture of equal amounts of water and ethanol, in which 0.2 wt.% CNF was dispersed as an adhesive. The stack was then hot-pressed under a pressure of 1 MPa and a temperature of 110°C using a hot-pressing machine (Shinto Metal Industries, Ltd., AYSR-5). The stacked films were then cut into a circular shape through a laser cutting machine (Makeblock, XTool P2).

4.2 | Thermal and Mechanical Stability

Thermogravimetric (TG) analyses of the absorber were carried out by a thermogravimetric analyzer (TA Instruments, TGA Q50) with nitrogen flow and heating rates of 60 mL min^{-1} and 10°C min^{-1}, respectively. Tensile tests for the three-layer absorber were performed using a universal testing machine (Shimadzu, EZ-SX) equipped with a 500 N load cell. A sheet of the three-layer absorber was conditioned under 23°C and 50% relative humidity for 2 days in advance. This conditioned sheet was cut into specimens with dimensions of 4 × 40 mm^2 by punching with a razor blade. The tab length, gauge length, and test speed

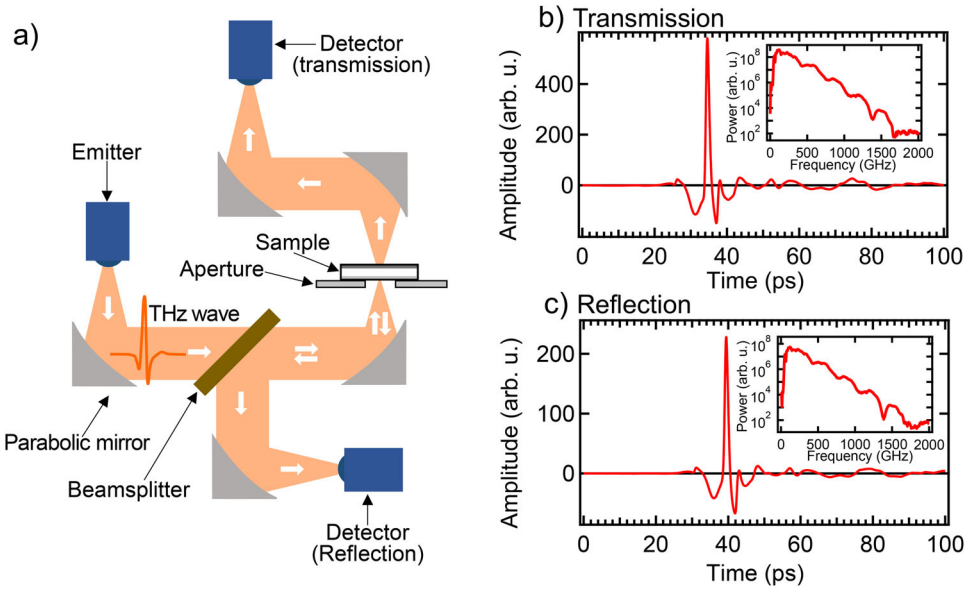

FIGURE 5 | (a) Schematic of the THz-TDS system used in this study. (b,c) Reference waveforms in the transmission and reflection configurations, respectively. The insets show their power spectra.

were set to 10 mm, 20 mm, and 2.0 mm min^{-1}, respectively. The tab regions of the specimens were covered with sandpaper and fixed with an adhesive. Three specimens were subjected to tensile testing.

4.3 | Measurement of the Electromagnetic Wave Responses

The schematic of the measurement setup for obtaining the dielectric function, SE, reflectance, and absorptance is shown in Figure 5a. This setup is based on a THz-TDS system with a pair of photoconductive antennas (TOPTICA Photonics, TeraFlash pro). The terahertz pulse emitted from a stripline photoconductive antenna was directed using off-axis parabolic mirrors. The wave transmitting a beamsplitter made of high-resistivity silicon was focused onto the sample. The wave passing through the sample was detected with a bowtie photoconductive antenna receiver to obtain dielectric functions and SEs. On the other hand, the wave reflected from the sample was partially reflected by the beamsplitter and then detected by the receiver to obtain the reflectance. To suppress water vapor absorption, the path of the terahertz beam was purged with dry air. All the measurements were done at room temperature. Figure 5b,c show the reference time-domain waveforms in the transmission and reflection configurations, corresponding to the signal transmitted through the aperture without a sample and the signal reflected from a silver mirror, respectively. Their insets show the power spectra of the reference waveforms, ranging from 100 to 2000 GHz.

4.4 | Calculation of Dielectric Function, SE, Reflectance, and Absorptance from THz-TDS Results

Dielectric functions of the CNT:CNF films were calculated from the transmission THz-TDS measurement results in the following way [52, 53]. The terahertz waveforms transmitting the sample and the reference waveform without a sample were measured, and their complex amplitudes (written as $\tilde{E}^T_{\mathrm{sam}}$ and $\tilde{E}^T_{\mathrm{ref}}$, respectively) were computed with Fourier transform. The complex transmission coefficient $\tilde{t}$ can be obtained as

$$\tilde{t} = \frac{\tilde{E}^T_{\mathrm{sam}}}{\tilde{E}^T_{\mathrm{ref}}} \tag{5}$$

On the other hand, the complex transmission coefficient $\tilde{t}$ is related to the complex refractive index $\tilde{n}$ as

$$\tilde{t} = \frac{4\tilde{n}}{(\tilde{n}+1)^2} \exp\left[i\frac{2\pi(\tilde{n}-1)fd}{c}\right] \sum_{m=0}^{M} \left\{ \left(\frac{\tilde{n}-1}{\tilde{n}+1}\right)^2 \exp\left[i\frac{4\pi\tilde{n}fd}{c}\right] \right\}^m \tag{6}$$

here, M is the maximum number of multiple reflections inside the sample in the measured terahertz waveform, and d is the sample thickness. Solving Equations (5) and (6) provides the complex refractive index $\tilde{n}$. Since the films for dielectric function measurements were thin, we took the limit of $M \to \infty$ to take all internal reflections inside the film into account. The complex dielectric function $\tilde{\varepsilon}$ was calculated from the complex refractive index as $\tilde{\varepsilon} = \tilde{n}^2$. Finally, the real part ε' and loss tangent $\tan\delta$ of the dielectric function were calculated as $\varepsilon' = \mathrm{Re}(\tilde{\varepsilon})$ and $\tan\delta = \mathrm{Im}(\tilde{\varepsilon})/\mathrm{Re}(\tilde{\varepsilon})$, respectively.

The power transmittance T was calculated from the complex transmission coefficient $\tilde{t}$ in Equation (5) as $T = |\tilde{t}|^2$, and the shielding effectiveness SE can be calculated from T using Equation (4). On the other hand, the reflectance R was calculated from the complex amplitude of the waveform reflected from the sample $\tilde{E}^R_{\mathrm{sam}}$ and the reference waveform reflected from a silver mirror $\tilde{E}^R_{\mathrm{ref}}$ as $R = |\tilde{E}^R_{\mathrm{sam}}/\tilde{E}^R_{\mathrm{ref}}|^2$. Then, the absorptance A was obtained as $A = 1 - T - R$. Note that the reflectance and absorptance in the manuscript are expressed in

percent, and the values are multiplied by 100 after the above calculations.

Acknowledgements

This work was partially supported by the Japan Society for the Promotion of Science (JSPS) Grants-in-Aid for Scientific Research (KAKENHI) Grant Nos. JP24H00317 and JP24H02232.

Conflicts of Interest

The authors declare no conflicts of interest.

Data Availability Statement

The data that support the findings of this study are available from the corresponding author upon reasonable request.

References

1. M. Z. Chowdhury, M. Shahjalal, S. Ahmed, and Y. M. Jang, "6G Wireless Communication Systems: Applications, Requirements, Technologies, Challenges, and Research Directions," *IEEE Open Journal of the Communications Society* 1 (2020): 957–975, https://doi.org/10.1109/OJCOMS.2020.3010270.

2. M. Alsabah, M. A. Naser, B. M. Mahmmod, et al., "6G Wireless Communications Networks: A Comprehensive Survey," *IEEE Access* 9 (2021): 148191–148243, https://doi.org/10.1109/ACCESS.2021.3124812.

3. J. Lee, H. Kim, and J. Oh, "Large-Aperture Metamaterial Lens Antenna for Multi-Layer MIMO Transmission for 6G," *IEEE Access* 10 (2022): 20486–20495, https://doi.org/10.1109/ACCESS.2022.3150037.

4. Z. Chen, C. Han, Y. Wu, et al., "Terahertz Wireless Communications for 2030 and Beyond: A Cutting-Edge Frontier," *IEEE Communications Magazine* 59 (2021): 66–72, https://doi.org/10.1109/MCOM.011.2100195.

5. Z. Wei, Z. Wang, J. Zhang, Q. Li, J. Zhang, and H. Y. Fu, "Evolution of Optical Wireless Communication for B5G/6G," *Progress in Quantum Electronics* 83 (2022): 100398, https://doi.org/10.1016/j.pquantelec.2022.100398.

6. H. Tao, C. M. Bingham, A. C. Strikwerda, et al., "Highly Flexible Wide Angle of Incidence Terahertz Metamaterial Absorber: Design, Fabrication, and Characterization," *Physical Review B* 78 (2008): 241103, https://doi.org/10.1103/PhysRevB.78.241103.

7. X. Cheng, R. Huang, J. Xu, and X. Xu, "Broadband Terahertz Near-Perfect Absorbers," *ACS Applied Materials & Interfaces* 12 (2020): 33352–33360, https://doi.org/10.1021/acsami.0c06162.

8. N. I. Landy, C. M. Bingham, T. Tyler, N. Jokerst, D. R. Smith, and W. J. Padilla, "Design, Theory, and Measurement of a Polarization-insensitive Absorber for Terahertz Imaging," *Physical Review B* 79 (2009): 125104, https://doi.org/10.1103/PhysRevB.79.125104.

9. J. Grant, Y. Ma, S. Saha, A. Khalid, and D. R. S. Cumming, "Polarization Insensitive, Broadband Terahertz Metamaterial Absorber," *Optics Letters* 36 (2011): 3476–3478, https://doi.org/10.1364/ol.36.003476.

10. V. C. Agulto, Z. Ling, Z. Zhao, et al., "Design and Fabrication of a Microcoil Metamaterial Absorber for the Sub-Terahertz Region," *Optics Letters* 48 (2023): 6324–6327, https://doi.org/10.1364/OL.502614.

11. Z. Shen, S. Li, Y. Xu, W. Yin, L. Zhang, and X. Chen, "Three-Dimensional Printed Ultrabroadband Terahertz Metamaterial Absorbers," *Physical Review Applied* 16 (2021): 014066, https://doi.org/10.1103/PhysRevApplied.16.014066.

12. D.-S. Kim, D.-H. Kim, S. Hwang, and J.-H. Jang, "Broadband Terahertz Absorber Realized by Self-Assembled Multilayer Glass Spheres," *Optics Express* 20 (2012): 13566–13572, https://doi.org/10.1364/OE.20.013566.

13. R. Yahiaoui, K. Hanai, K. Takano, et al., "Trapping Waves With Terahertz Metamaterial Absorber Based on Isotropic Mie Resonators," *Optics Letters* 40 (2015): 3197–3200, https://doi.org/10.1364/OL.40.003197.

14. D. Yang, C. Zhang, X. Ju, Y. Ji, and C. Lan, "Multi-Resonance and Ultra-Wideband Terahertz Metasurface Absorber Based on Micro-Template-Assisted Self-Assembly Method," *Optics Express* 28 (2020): 2547–2556, https://doi.org/10.1364/OE.381927.

15. S. Yin, J. Zhu, W. Xu, et al., "High-Performance Terahertz Wave Absorbers Made of Silicon-Based Metamaterials," *Applied Physics Letters* 107 (2015): 073903, https://doi.org/10.1063/1.4929151.

16. X. Liu, K. Fan, I. V. Shadrivov, and W. J. Padilla, "Experimental Realization of a Terahertz All-Dielectric Metasurface Absorber," *Optics Express* 25 (2017): 191–201, https://doi.org/10.1364/OE.25.000191.

17. K. Fan, J. Y. Suen, X. Liu, and W. J. Padilla, "All-Dielectric Metasurface Absorbers for Uncooled Terahertz Imaging," *Optica* 4 (2017): 601–604, https://doi.org/10.1364/OPTICA.4.000601.

18. A. Namai, M. Yoshikiyo, K. Yamada, et al., "Hard Magnetic Ferrite With a Gigantic Coercivity and High Frequency Millimetre Wave Rotation," *Nature Communications* 3 (2012): 1035, https://doi.org/10.1038/ncomms2038.

19. G. Li, O. Stefanczyk, K. Kumar, Y. Mineo, K. Nakabayashi, and S.-I. Ohkoshi, "Low-Frequency Sub-Terahertz Absorption in Hg II −XCN−Fe II (X=S, Se) Coordination Polymers," *Angewandte Chemie International Edition* 62 (2023), https://doi.org/10.1002/anie.202214673.

20. Z. Huang, H. Chen, Y. Huang, et al., "Ultra-Broadband Wide-Angle Terahertz Absorption Properties of 3D Graphene Foam," *Advanced Functional Materials* 28 (2018): 1704363, https://doi.org/10.1002/adfm.201704363.

21. Z. Barani, K. Stelmaszczyk, F. Kargar, et al., "Efficient Terahertz Radiation Absorption by Dilute Graphene Composites," *Applied Physics Letters* 120 (2022): 063104, https://doi.org/10.1063/5.0079891.

22. K. Zeranska, K. Filak, K. Wilczynski, et al., "Graphene-Based Thermoplastic Composites as Extremely Broadband and Frequency-Dependent EMI Absorbers for Multifunctional Applications," *ACS Applied Electronic Materials* 4 (2022): 4463–4470, https://doi.org/10.1021/acsaelm.2c00722.

23. W. W. Salisbury, "Absorbent Body of Electromagnetic Waves," (U. S. Patent), *2 599 944A* (1952).

24. A. J. Gatesman, A. Danylov, T. M. Goyette, et al., "Terahertz Behavior of Optical Components and Common Materials," *Proceedings SPIE* 6212 (2006):62120E, https://doi.org/10.1117/12.668384.

25. J. M. Woo, M.-S. Kim, H. W. Kim, and J.-H. Jang, "Graphene Based Salisbury Screen for Terahertz Absorber," *Applied Physics Letters* 104 (2014): 081106, https://doi.org/10.1063/1.4866665.

26. Y. Gu, X. Xu, F. Wang, et al., "Salisbury Screen Terahertz Absorber Formed With an Insulator: 4- N , N -Dimethylamino-4′- N′-methyl-Stilbazolium Tosylate (DAST)," *ACS Omega* 4 (2019): 9204–9210, https://doi.org/10.1021/acsomega.9b00013.

27. K. Abe, S. Iwamoto, and H. Yano, "Obtaining Cellulose Nanofibers With a Uniform Width of 15 Nm From Wood," *Biomacromolecules* 8 (2007): 3276–3278, https://doi.org/10.1021/bm700624p.

28. A. Isogai, T. Saito, and H. Fukuzumi, "TEMPO-Oxidized Cellulose Nanofibers," *Nanoscale* 3 (2011): 71–85, https://doi.org/10.1039/C0NR00583E.

29. M. Nogi and H. Yano, "Transparent Nanocomposites Based on Cellulose Produced by Bacteria Offer Potential Innovation in the Electronics Device Industry," *Advanced Materials* 20 (2008): 1849–1852, https://doi.org/10.1002/adma.200702559.

30. T. Kasuga, H. Yagyu, K. Uetani, H. Koga, and M. Nogi, "Return to the Soil″ Nanopaper Sensor Device for Hyperdense Sensor Networks," *ACS Applied Materials & Interfaces* 11 (2019): 43488–43493, https://doi.org/10.1021/acsami.9b13886.

31. T. Kasuga, A. Mizui, H. Koga, and M. Nogi, "Wirelessly Powered Sensing Fertilizer for Precision and Sustainable Agriculture," *Advanced Sustainable Systems* 8 (2024): 2300314, https://doi.org/10.1002/adsu.202300314.

32. A. Iwatake, M. Nogi, and H. Yano, "Cellulose Nanofiber-Reinforced Polylactic Acid," *Composites Science and Technology* 68 (2008): 2103–2106, https://doi.org/10.1016/j.compscitech.2008.03.006.

33. A. Nakanishi, N. Kanno, and H. Satozono, "Nondestructive and Noncontact Evaluation of Cellulose Nanofiber-reinforced Composites Using Terahertz Time-Domain Spectroscopy," *Scientific Reports* 12 (2022): 19284, https://doi.org/10.1038/s41598-022-23865-8.

34. T. Kasuga, T. Saito, H. Koga, and M. Nogi, "One-Pot Hierarchical Structuring of Nanocellulose by Electrophoretic Deposition," *ACS Nano* 16 (2022): 18390–18397, https://doi.org/10.1021/acsnano.2c06392.

35. T. Kasuga, H. Yagyu, K. Uetani, H. Koga, and M. Nogi, "Cellulose Nanofiber Coatings on Cu Electrodes for Cohesive Protection Against Water-Induced Short-Circuit Failures," *ACS Applied Nano Materials* 4 (2021): 3861–3878, https://doi.org/10.1021/acsanm.1c00267.

36. V. Petrov, T. Kurner, and I. Hosako, "IEEE 802.15.3d: First Standardization Efforts for Sub-Terahertz Band Communications Toward 6G," *IEEE Communications Magazine* 58 (2020): 28–33, https://doi.org/10.1109/MCOM.001.2000273.

37. C.-X. Wang, X. You, X. Gao, et al., "On the Road to 6G: Visions, Requirements, Key Technologies, and Testbeds," *IEEE Communications Surveys & Tutorials* 25 (2023): 905–974, https://doi.org/10.1109/COMST.2023.3249835.

38. H. Xu, X. Yin, M. Li, et al., "Ultralight Cellular Foam From Cellulose Nanofiber/Carbon Nanotube Self-Assemblies for Ultrabroad-Band Microwave Absorption," *ACS Applied Materials & Interfaces* 11 (2019): 22628–22636, https://doi.org/10.1021/acsami.9b03731.

39. Z. Zeng, C. Wang, G. Siqueira, et al., "Nanocellulose-MXene Biomimetic Aerogels With Orientation-Tunable Electromagnetic Interference Shielding Performance," *Advanced Science* 7 (2020): 2000979, https://doi.org/10.1002/advs.202000979.

40. R. Zhang, N. Wu, F. Pan, et al., "Scalable Manufacturing of Light, Multifunctional Cellulose Nanofiber Aerogel Sphere With Tunable Microstructure for Microwave Absorption," *Carbon* 203 (2023): 181–190, https://doi.org/10.1016/j.carbon.2022.11.055.

41. T. Mai, L. Chen, Q. Liu, Z. Guo, and M. Ma, "Zeolitic Imidazolate Frameworks Derived Magnetic Nanocage/MXene/Nanocellulose Bilayer Aerogels for Low Reflection Electromagnetic Interference Shielding and Light-to-Heat Conversion," *Advanced Functional Materials* 35 (2025): 2417947, https://doi.org/10.1002/adfm.202417947.

42. T. Mai, L. Chen, P.-L. Wang, Q. Liu, and M.-G. Ma, "Hollow Metal–Organic Framework/MXene/Nanocellulose Composite Films for Giga/Terahertz Electromagnetic Shielding and Photothermal Conversion," *Nano-Micro Letters* 16 (2024): 169, https://doi.org/10.1007/s40820-024-01386-5.

43. J. Niu, X. Chao, H. Lian, J. Luo, and L. Qi, "Machine Learning and Droplet-Based Printing Accelerating the Achievement of Flexible Terahertz Metamaterial Absorber," *Chemical Engineering Journal* 519 (2025): 165123, https://doi.org/10.1016/j.cej.2025.165123.

44. V. C. Agulto, K. Toya, T. N. K. Phan, et al., "Anisotropic Complex Refractive Index of β-Ga_2O_3 Bulk and Epilayer Evaluated by Terahertz Time-Domain Spectroscopy," *Applied Physics Letters* 118 (2021), https://doi.org/10.1063/5.0031531.

45. J. Wang, W. Cai, W. Lu, et al., "Observation of 2D-Magnesium-Intercalated Gallium Nitride Superlattices," *Nature* 631 (2024): 67–72, https://doi.org/10.1038/s41586-024-07513-x.

46. H. Nishimura, N. Minami, and R. Shimano, "Dielectric Properties of Single-Walled Carbon Nanotubes in the Terahertz Frequency Range," *Applied Physics Letters* 91 (2007): 011108, https://doi.org/10.1063/1.2753747.

47. D. Nuzhnyy, M. Savinov, V. Bovtun, et al., "Broad-Band Conductivity and Dielectric Spectroscopy of Composites of Multiwalled Carbon Nanotubes and Poly(ethylene terephthalate) Around Their Low Percolation Threshold," *Nanotechnology* 24 (2013): 055707, https://doi.org/10.1088/0957-4484/24/5/055707.

48. W. Zhang, R. Mi, and V. Khilkevich, "3D Printed Multilayer Microwave Absorber," in 2022 IEEE International Symposium on Electromagnetic Compatibility & Signal/Power Integrity (IEEE, 2022), https://doi.org/10.1109/EMCSI39492.2022.9889603.

49. Z. Awang, F. A. M. Zaki, N. H. Baba, A. S. Zoolfakar, and R. A. Bakar, "A Free-Space Method for Complex Permittivity Measurement of Bulk and Thin Film Dielectrics at Microwave Frequencies," *Progress In Electromagnetics Research B* 51 (2013): 307–328, https://doi.org/10.2528/PIERB13031509.

50. H. Fukuzumi, T. Saito, Y. Okita, and A. Isogai, "Thermal Stabilization of TEMPO-Oxidized Cellulose," *Polymer Degradation and Stability* 95, no. 9 (2010): 1502–1508, https://doi.org/10.1016/j.polymdegradstab.2010.06.015.

51. S. Ishioka, N. Isobe, T. Hirano, N. Matoba, S. Fujisawa, and T. Saito, "Fully Wood-Based Transparent Plates With High Strength, Flame Self-Extinction, and Anisotropic Thermal Conduction," *ACS Sustainable Chemistry & Engineering* 11, no. 6 (2023): 2440–2448, https://doi.org/10.1021/acssuschemeng.2c06344.

52. J. Neu and C. A. Schmuttenmaer, "Tutorial: An Introduction to Terahertz Time Domain Spectroscopy (THz-TDS)," *Journal of Applied Physics* 124, no. 23 (2018): 231101, https://doi.org/10.1063/1.5047659.

53. M. Hangyo, M. Tani, and T. Nagashima, "Terahertz Time-Domain Spectroscopy of Solids: A Review," *International Journal of Infrared and Millimeter Waves* 26, no. 12 (2005): 1661–1690, https://doi.org/10.1007/s10762-005-0288-1.

Supporting Information

Additional supporting information can be found online in the Supporting Information section.

Supporting file: admt70559-sup-0001-SuppMat.pdf